https://doi.org/10.5194/egusphere-2026-3698
Preprint. Discussion started: 2 July 2026

Resolving heterogeneous structure and finite scattering in clouds and precipitation with ultra-high-resolution lidar

Grant J. Kirchhoff[1], Matthew Hayman[2], Jeffrey P. Thayer[1], and Bryce H. Garby[1,2]

[1]University of Colorado Boulder, Ann and H.J. Smead Aerospace Engineering Sciences Department, Boulder, Colorado 80309, USA
[2]NSF National Center for Atmospheric Research, Earth Observing Lab, Boulder, Colorado 80303, USA

Correspondence: Grant J. Kirchhoff (grant.kirchhoff@colorado.edu)

Abstract. Lidar is as a key observational tool for cloud profiling, enabling measurements near and within clouds at finer spatiotemporal resolutions than many other remote sensors. However, most atmospheric lidar retrievals rely on the volume backscatter lidar equation, which treats the received signal as a volumetric average over the sampled particle field. This approximation assumes that the average particle-backscatter behavior within the sample volume is representative of the underlying ensemble mean. This study shows that this condition is well satisfied only in locally homogeneous, high particle-occupancy regimes, which are not always present in clouds. Ultra-high-resolution lidar observations at $11\,\mathrm{cm} \times 70\,\mu\mathrm{s}$ in range and time reveal sparsely populated and inhomogeneous cloud regions that violate these assumptions. These observations motivate a statistical formulation of volume scattering, showing that the classical volume-average interpretation emerges as the homogeneous, high-occupancy limit of finite-particle scattering. The formulation enables an analytic investigation of how cloud microphysical properties and instrument parameters contribute to measurement variability, demonstrating how sparse scattering within the sample volume can weaken the volumetric interpretation. Finally, two retrieval approaches are demonstrated that leverage ultra-high-resolution lidar data to estimate cloud-relevant parameters, including hydrometeor kinematics and photon flux, at the single-hydrometeor scale. This work clarifies the conditional limits of the volumetric approximation in cloud lidar and motivates new lidar designs and retrieval strategies that exploit individual particle-scattering contributions and their statistical nature.

1 Introduction

Clouds play a central role in Earth's weather and climate system by regulating radiation, precipitation, and atmospheric dynamics across scales. Despite this importance, many of the microphysical processes that govern cloud evolution and cloud-radiative properties remain incompletely understood, contributing to persistent uncertainty in climate and weather predictions (Morrison et al., 2020; Fan et al., 2016; Zelinka et al., 2020; IPCC, 2021). Improving observational constraints on these processes therefore remains essential for understanding how clouds evolve and interact with their environment.

https://doi.org/10.5194/egusphere-2026-3698
Preprint. Discussion started: 2 July 2026

Lidar has been identified as a key observational tool for cloud profiling, with its high sensitivity to cloud particles making it well suited for high-resolution remote measurements of clouds (National Research Council, 2009; Winker et al., 2009; Wang and Menenti, 2021). Lidar-based retrievals provide estimates of key parameters, such as cloud phase (Crosbie et al., 2025; Sassen, 1991; Hu et al., 2009), optical radiative properties (Young et al., 2018; Comstock and Sassen, 2001), and microphysical properties (Jimenez et al., 2020), but are limited to bulk representations of the cloud field. This is because operational cloud-lidar products typically average over sample volumes that exceed tens of meters in range and seconds in time (Flynn et al., 2020; Griesche et al., 2024). Yet many cloud microphysical processes occur on much smaller scales: droplet activation, condensational growth, and collision-coalescence involve particle-scale lengths spanning micrometers to millimeters; with many turbulent and phase-relaxation timescales ranging from subsecond to multiple seconds (Shaw, 2003; Lehmann et al., 2009). While coarse averaging over highly variable structure suppresses fine-scale variability in cloud measurements through smoothing, it limits the ability to relate the measured signal to the underlying cloud structure. This effect is not simply a consequence of reduced resolution; it reflects a loss of information caused by averaging over complex particle fields.

Standard atmospheric- and cloud-lidar retrievals are commonly formulated in terms of volume optical quantities, including attenuated backscatter, volume backscatter, and volume extinction (Measures, 1984; CALIPSO Science Team and Lidar Science Working Group, 2007; Fernald, 1984). This interpretation is well posed for measurements of well-mixed, high-occupancy media, such as molecular Rayleigh-scattering regions, where the number of scatterers is high enough to ensure negligible fluctuations about the volume mean. However, for clouds, the limits of this continuum or volume-average approximation are less explicit. It has been observed that clouds can exhibit microphysical variability on scales that are smaller than standard lidar sample volumes (Kostinski and Shaw, 2001; Knyazikhin et al., 2005; Beals et al., 2015; Glienke et al., 2020; Thiede et al., 2025), suggesting that particle-field properties (such as degree of sparsity and inhomogeneity) and instrument parameters (such as laser pulse width, beam divergence, and wavefront), influence the validity of the volume-average approximation. This limitation is likely most important near entraining cloud edges, where heterogeneous mixing can produce strong small-scale variability (Yeom et al., 2023), and in tenuous ice clouds, where low particle concentrations (Beswick et al., 2015) may make a finite sample less representative of a homogeneous medium. Furthermore, unresolved cloud heterogeneity is increasingly recognized as an important constraint on the retrieval of cloud optical properties, because retrieval algorithms often rely on simplified homogeneous or one-dimensional representations of cloud structure (Arola et al., 2022; Alkasem et al., 2017).

Ultra-high-resolution lidar measurements provide a way to probe cloud backscatter at scales closer to the underlying particle field, where conventional-resolution returns may be influenced not only by their bulk optical properties but also by sparse sampling and small-scale heterogeneity within the sampled volume (Shaw, 2003). Recent advances in time-correlated single-photon-counting lidar have enabled cloud observations at submeter range resolution (Barton-Grimley et al., 2018; Yang et al., 2023). These studies demonstrate increasing interest in ultra-high-resolution lidar as a cloud sensor and motivate its use for retrieving microphysical parameters at fine scales (Yang et al., 2024, 2025; Zhu et al., 2024). This work extends these efforts by using ultra-high-resolution lidar to not only demonstrate the method's ability to resolve fine-scale features in clouds, but also to examine how discreteness (i.e., finite-particle occupancy and heterogeneous particle arrangement) can produce scattering behavior that is not necessarily captured by the volumetric approximation. In this study, we use ultra-high-resolution cloud

https://doi.org/10.5194/egusphere-2026-3698
Preprint. Discussion started: 2 July 2026

lidar observations to examine when the conventional volumetric interpretation of lidar measurements is valid and when finite or heterogeneous scattering becomes important.

To accomplish this, we first present ultra-high-resolution lidar observations that reveal discrete, heterogeneous, and finite-scattering features in clouds. Next, we develop a statistical framework that connects discrete-particle scattering to the classical volume backscatter lidar equation and identifies the conditions under which the volumetric interpretation is recovered. Finally, we demonstrate retrievals of single-hydrometeor kinematics and flux in sparse clouds and precipitation, illustrating how ultra-high-resolution lidar enables measurements in regimes where cloud constituents are resolved as individual scatterers.

2 Measurement approach

The observations presented in this study were collected using an ultra-high-resolution elastic backscatter lidar. The system is ground based and zenith pointing, providing continuous sampling of clouds from below. By measuring elastically scattered photons at the transmitted wavelength of 532 nm, the instrument achieves high sensitivity to cloud particles while maintaining a comparatively simple architecture. Several design features enable measurements at scales substantially finer than those of conventional cloud lidars. The transmitter employs short laser pulses (750 ps, or 11 cm in range, at full-width half-maximum) at a high repetition rate (14.3 kHz), yielding simultaneous high temporal resolution (70 us) and an unambiguous range suitable for tropospheric cloud observations (up to 10.4 km). Combined with moderate transmitted power (35 mW), these characteristics provide strong cloud returns with signal levels well above molecular and nighttime background contributions.

On the receiver side, single-photon-counting detectors are coupled with time-tag acquisition electronics that record the arrival time of every detected photon relative to each transmitted pulse (Becker, 2005). This approach preserves the full temporal information content of the measurement and yields an effective timing resolution of 25 ps, or 4 mm in range. Together, these capabilities enable direct observation of cloud structure and scattering processes at spatiotemporal scales that are typically unresolved by conventional atmospheric lidar systems. The most important system parameters are summarized in Tab. 1.

3 Observational motivation

We present observations illustrating how the interpretation of cloud-lidar signals depends jointly on observational resolution and the underlying particle field, with fine-scale measurements revealing discrete scatter structure that is obscured through conventional averaging. This concept is depicted in Fig. 1, which shows a typical cirrus cloud measurement at ultra-high resolution. In this paper, “ultra-high resolution” is defined as spatiotemporal sampling finer than that of standard cloud lidars, specifically range and temporal resolutions below 1 m and 1 s, respectively. At this resolution, gradients in apparent backscatter intensity reveal nonuniform features, including cloud-edge transitions and variability in particle concentration.

Fig. 1 shows how ultra-high resolution lidar resolves fine-scale structures and dynamics present in clouds that are missed at coarser scales. In Fig. 1a.1 and b.1, structures and dynamical processes, like filaments and internal mixing, are resolved. To compare this with what a standard “high-resolution” cloud lidar would observe, the data was averaged to 10 m x 10 s in Fig. 1a.2

https://doi.org/10.5194/egusphere-2026-3698
Preprint. Discussion started: 2 July 2026

Table 1. Important lidar parameters.

Component	Parameter	Value
Transmitter	Wavelength	532 nm
	Pulse width (full-width half max)	750 ps (11 cm in range)
	Pulse rate	14.3 kHz (70 µs period)
	Beam width	2.5 cm
	Beam full-angle divergence	200 µrad
	Gaussian M^2	< 1.2
	Output energy	2.45 µJ
	Unambiguous range	10.4 km
Receiver	Aperture	20.3 cm
	Full field of view	1.4 mrad
	Filter bandwidth	4 nm
	Quantum efficiency	50%
	Gain ratio	90:1
	Detector deadtime	29.5 ns (high gain), 31.8 ns (low gain)
Acquisition	Time-tag resolution	25 ps (4 mm in range)
	Board deadtime	< 25 ns

and b.2. The data were then converted to photon flux (or photon arrival rate) using the standard estimator $\hat{\Phi}_{ij} = k_{ij}/(M_j \Delta t)$, where $\hat{\Phi}$ represents the estimated flux at the ij-th bin, k is the number of photon counts, M is the number of integrated laser shots, and Δt is the range-bin size (in units of time). While averaging data provides a simple way to reduce noise, it does so by smoothing over fine-scale structures in both the atmosphere and lidar signals. When atmospheric features are spatially or temporally correlated, averaging along one dimension can diminish the effective resolution gained in the other. For example, averaging over time to improve range-resolved signal quality can smear temporally evolving structures, making high range resolution less physically interpretable. The effect of averaging also depends on the motion of the laser beam relative to the cloud field. For scanning lidars or moving platforms, such as airplanes or satellites, temporal integration corresponds to spatial averaging along the beam direction or platform trajectory. This motion-induced averaging can smear fine-scale cloud structure and places stricter limits on allowable integration times than in static ground-based observations.

The first effect to discuss is that conventional averaging obscures heterogeneous structure, limiting the ability to relate lidar signals to the underlying properties in clouds. Fig. 1a.2 and b.2 illustrate this point, where nonuniform scatter structures are smoothed over and appear locally homogeneous. Here, “homogeneous” describes a particle field whose underlying statistical distribution is uniform in space over the measurement scale, and “heterogeneous” to describe one with a nonuniform spatial distribution. The perceived continuity is not a reflection of underlying uniformity but instead an artifact of averaging. For media that are homogeneous over the measurement volume, such as molecular scattering from gases under appropriate ergodic con-

https://doi.org/10.5194/egusphere-2026-3698
Preprint. Discussion started: 2 July 2026

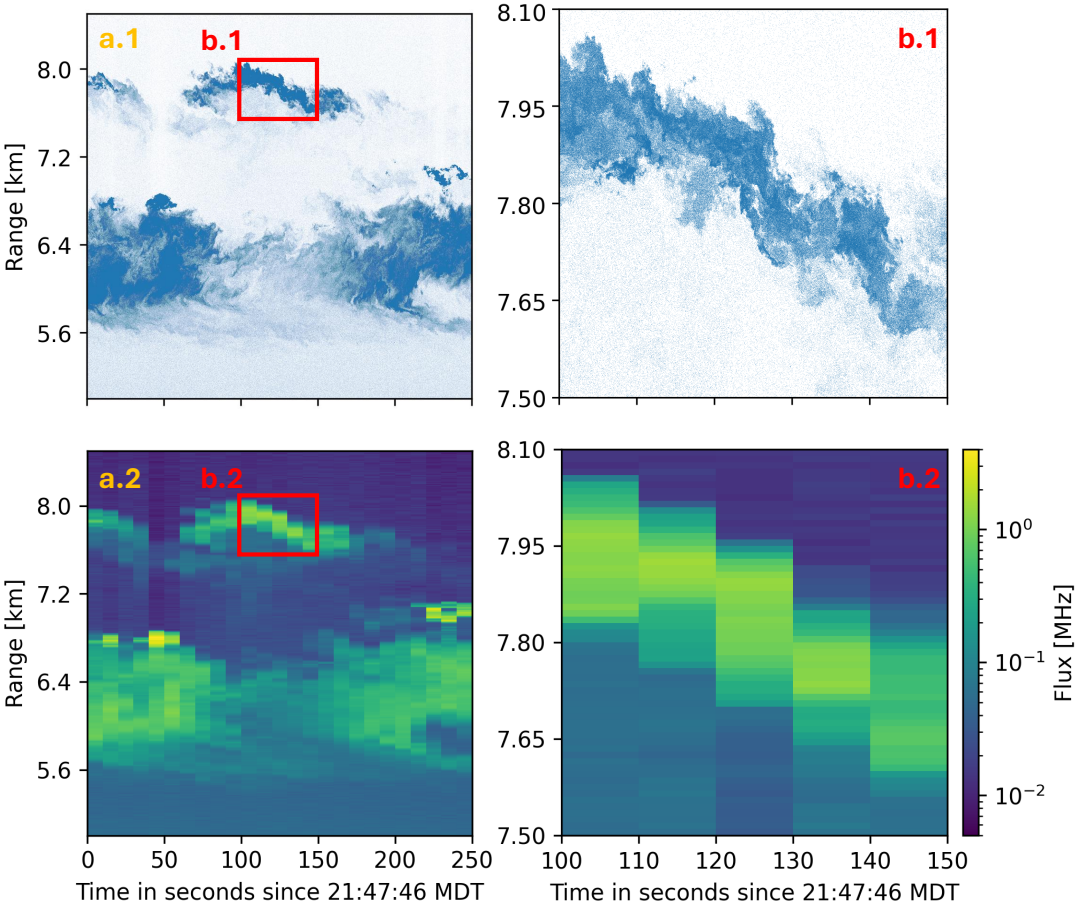

Figure 1. Ultra-high-resolution lidar observations of cloud structure shown at native and averaged resolutions. Panels (a.1) and (b.1) show individual photon detection events plotted in time and range at the native acquisition resolution of 4 mm in range and 70 µs in time, where dot density visually represents backscatter intensity. Panels (a.2) and (b.2) show the same measurements averaged to 10 m × 10 s and converted to photon flux.

ditions, the volume-averaged return provides a meaningful representation of the sampled medium (Measures, 1984). In cloud and aerosol features, however, this local homogeneity condition may not be satisfied. Heterogeneity can cause the measured return to depend on the particular arrangement of scatterers within the illuminated volume, thereby limiting the applicability of the classical volume-backscatter lidar equation. Furthermore, small-scale dynamics can organize droplet positions into spatially correlated clusters, even within otherwise statistically homogeneous cloud regions (Kostinski and Shaw, 2001). The volume backscatter formulation implicitly assumes that the scattering medium varies only weakly over the measurement scale,

https://doi.org/10.5194/egusphere-2026-3698
Preprint. Discussion started: 2 July 2026

meaning that, under nonuniform illumination, these effects become important since the lidar return weights different parts of the sampled volume unequally.

In addition to suppressing spatial heterogeneity, averaging also obscures finite-sampling effects due to discrete particles. In this paper, "finite sampling" is defined as backscatter that is governed by a low number of scatterers relative to the measurement volume. This effect is exemplified in an ice cloud example in Fig. 2. Fig. 2b.1 shows fine-scale, discrete clustering that is granular and tightly grouped, consistent with sparse hydrometeors within the measurement volume. When averaged to 10 m x 1 s in Fig. 2b.2, the discrete clustering is obscured, and the scene becomes visually indistinguishable from a continuum-like field. The underlying discreteness reemerges only after binning to scales that are comparable to or smaller than the interparticle spacing, like in Fig. 2b.3 and b.4. However, the apparent randomness of the particle configuration in Fig. 2b.1 should not be interpreted as detector or photon-counting shot noise. Instead, it reflects finite-particle sampling variability, a result of stochastic fluctuations in particle occurrences at low scatterer concentration. This phenomenon can produce signals that resemble those from heterogeneous volumes, even when the underlying statistical parameters describing the field are homogeneous. Therefore, sampling variability should not be conflated with physical heterogeneity.

Taken together, these results indicate that the applicability of the standard volume backscatter lidar equation depends jointly on the observational resolution and the statistical realization of the scattering medium within the sample volume. The lidar equation describes backscatter from a continuous, homogeneous medium, where the scatterer density is sufficiently high that discrete scattering events can be replaced by their ensemble mean. While this assumption is generally valid in high-density, well-mixed media such as gases, it can break down in clouds, where the droplet field can be sparse or heterogeneous relative to the measurement volume. The conditions under which this approximation fails are not well defined, particularly in clouds where spatiotemporal variability and finite-sampling effects are intertwined. In the following section, we address this gap by deriving the volume backscatter lidar equation from discrete scattering statistics, providing the underlying theory for identification of regimes in which the continuum approximation ceases to be valid. This provides a stochastic framework for resolution-dependent interpretation of cloud lidar observations.

4 Statistical foundation of volume backscatter

4.1 Deriving volume backscatter from discrete scatter theory

We now show that the traditional volume backscatter lidar equation emerges as a high-occupancy limit of the discrete formulation under a set of implicit statistical assumptions. This derivation makes these assumptions explicit and clarifies how the classical lidar equation emerges as a well-constrained limit of the underlying discrete scattering process.

To begin, the cloud particle field is modeled as a point process

$$\Xi = \{(X_i, Y_i, Z_i, S_i)\}_{i=1}^{N}, \tag{1}$$

https://doi.org/10.5194/egusphere-2026-3698
Preprint. Discussion started: 2 July 2026

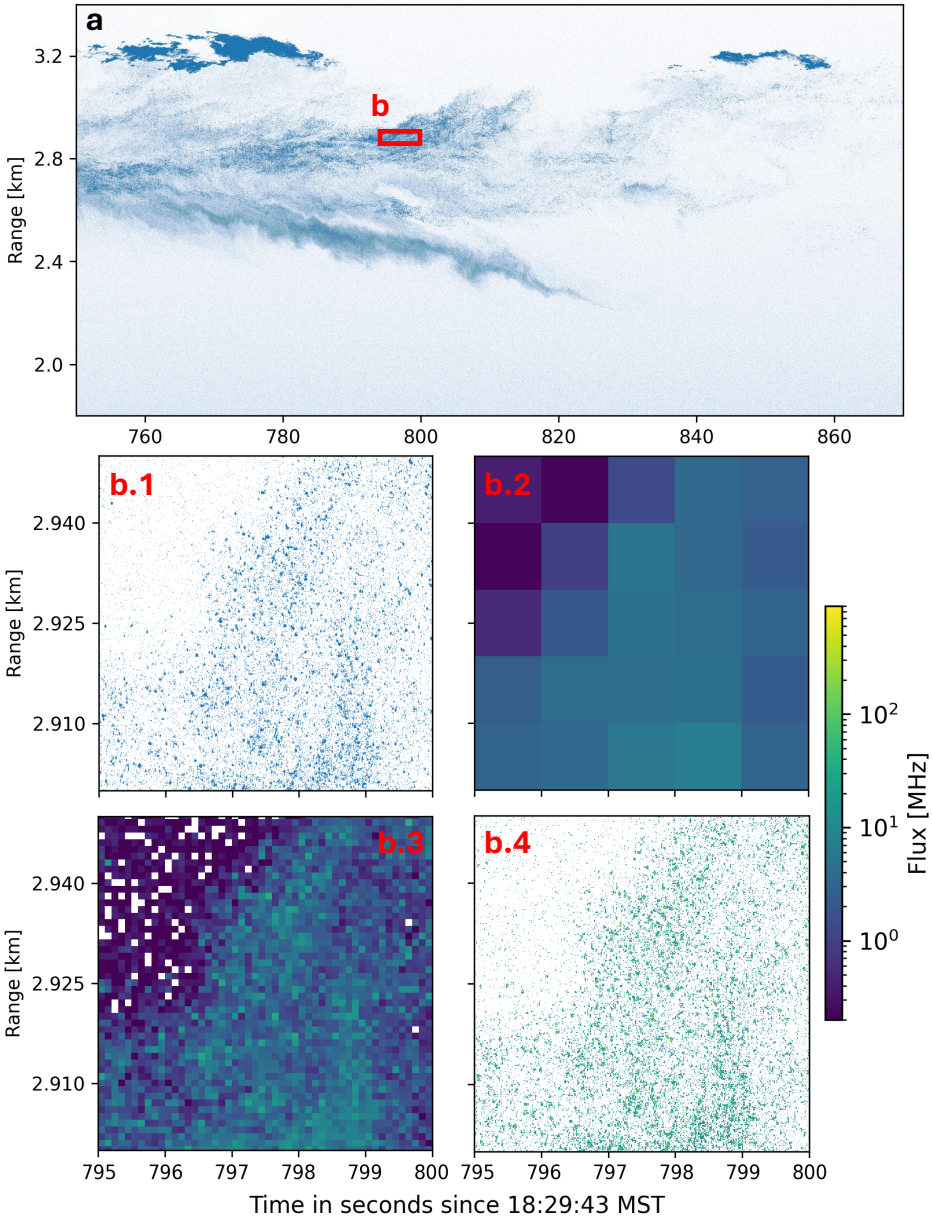

Figure 2. Ice cloud observation illustrating finite-particle sampling effects in ultra-high-resolution lidar measurements. Panel (b.1) shows individual photon detection events plotted in time and range, revealing granular, tightly grouped scattering features consistent with discrete hydrometeor contributions. Panel (b.2) shows the same scene averaged to $10\,\mathrm{m} \times 1\,\mathrm{s}$. Panels (b.3) and (b.4) show the data binned at progressively finer scales, i.e., $1\,\mathrm{m} \times 0.1\,\mathrm{s}$ and $0.1\,\mathrm{m} \times 0.01\,\mathrm{s}$, respectively.

https://doi.org/10.5194/egusphere-2026-3698
Preprint. Discussion started: 2 July 2026

where (X, Y, Z) denotes the particle's spatial location, S its size, and N the number of particles. A single realization of this process is denoted by

$$\boldsymbol{\xi} = \{(x_i, y_i, z_i, s_i)\}_{i=1}^{N}. \tag{2}$$

Following the single-scattering treatment of particle scattering and standard elastic lidar equation geometry (Measures, 1984), the received power at range R for a given particle configuration is given by

$$P(R|\boldsymbol{\Xi} = \boldsymbol{\xi}) = \left[\sum_{i=1}^{N} I(x_i, y_i, z_i) \frac{d\sigma_b}{d\Omega}(s_i)\right] A_{rx} R^{-2} O(R) \eta T(R)^2, \tag{3}$$

where $I(x, y, z)$ is the range-filtered irradiance field evaluated at the particle location, $d\sigma_b/d\Omega$ is the differential backscatter cross section (Bohren and Huffman, 1983), A_{rx} is the receiver aperture area, $O(R)$ is the geometric overlap function, η is the receiver efficiency, and $T(R)^2$ is the two-way transmission loss. In this derivation, we assume that the received signal is given by linear superposition of single-particle scattering contributions, such that multiple scattering, coherent interference, particle-scattering dependence, and inter-bin correlations are treated as negligible. These effects may be considered non-negligible under specific conditions, like optically dense clouds, which would require a more comprehensive assessment (Eloranta, 1998; Bissonnette, 2005).

The range-filtered irradiance field combines the transmitted field and the receiver range bin into a single effective term by projecting the propagated field onto the finite range bin, allowing us to reduce the beam and receiver resolution parameters into a single statistical description. This irradiance field is obtained by convolving the transmitted irradiance I_{tx} with a finite boxcar function of width ΔR:

$$I(x, y, z) = \frac{1}{\Delta R}(I_{tx} * h)(x, y, z) = \frac{1}{\Delta R} \int_{z}^{z+\Delta R} I_{tx}(x, y, z')dz', \tag{4}$$

where $(*)$ is defined as convolution strictly in z and the boxcar kernel is defined as

$$h(\zeta) = \Pi\left(\frac{\zeta}{\Delta R}\right) \triangleq \begin{cases} 1, & 0 \le \zeta \le \Delta R, \\ 0, & \text{otherwise.} \end{cases} . \tag{5}$$

It is important that ΔR is assumed small enough for the given beam wavefront that diffraction effects are considered negligible over the range extent.

We then invoke a high-occupancy (law-of-large-numbers) regime in which the measurement volume contains a sufficiently large number of independent and identical scattering contributions. Under this assumption, the received signal is self-averaging, such that a single realization is well approximated by its ensemble mean, i.e., $P(R|\boldsymbol{\Xi} = \boldsymbol{\xi}) \approx \langle P(R) \rangle$, and fluctuations about the mean are relatively negligible. To calculate the ensemble mean, the received power is treated as a random variable and consider its expectation:

$$\langle P(R) \rangle = \mathbb{E}_{\boldsymbol{\Xi}}[P(R|\boldsymbol{\Xi})] = C(R)\mathbb{E}_{\boldsymbol{\Xi}}\left[\sum_{i=1}^{N} I(x_i, y_i, z_i) \frac{d\sigma_b}{d\Omega}(s_i)\right], \tag{6}$$

https://doi.org/10.5194/egusphere-2026-3698
Preprint. Discussion started: 2 July 2026

where ΔR is assumed small enough to ensure $C(R) = A_{rx}R^{-2}O(R)\eta T^2(R)$ is approximately constant over the range extent. We then invoke Campbell's theorem, which allows us to express the expectation of a sum over a point process in terms of an integral against its intensity measure (Last and Penrose, 2017), yielding

$$\langle P(R)\rangle = C(R)\int_D I(x,y,z)\frac{d\sigma_b}{d\Omega}(s)\Lambda(\bar{\xi})d\bar{\xi}, \tag{7}$$

where $\bar{\xi} = (x,y,z,s)$ is a coordinate in the four-dimensional domain $D \subset \mathbb{R}^3 \times \mathbb{R}_+$, spanning three-dimensional physical space and particle size. Here, $s > 0$ restricts the domain to physically admissible particle sizes, and $\Lambda(\bar{\xi})$ is the point-process intensity, so that $\Lambda(\bar{\xi})d\bar{\xi}$ gives the expected number of particles in the state-space element $d\bar{\xi} = dx\,dy\,dz\,ds$.

Next, we impose two assumptions: (1) spatial and size statistics are separable and (2) particles are uniformly distributed over some volume V, allowing the intensity function to be rewritten as

$$\Lambda(\bar{\xi}) = \frac{\langle N\rangle}{V}g(s) \equiv n(s), \tag{8}$$

where $\langle N\rangle$ is the expected number of particles in the volume and $g(s)$ is the size probability density function (e.g., gamma or modified-gamma distribution commonly used for cloud particle populations) (Miles et al., 2000). This intensity function is thus equivalent to the particle or droplet size distribution $n(s)$. Recognizing the continuous form of the volume backscatter coefficient

$$\beta \triangleq \int_0^\infty \frac{d\sigma_b}{d\Omega}(s)n(s)ds \tag{9}$$

allows Eq. 7 to be written as

$$\langle P(R)\rangle = \beta C(R)\int_V I(x,y,z)dV. \tag{10}$$

Now we assume that the transmitted pulse is sufficiently short relative to the range bin width ΔR such that it can be approximated as range localized, i.e., $I(x,y,z) \approx I_{tx}(x,y,R)\Pi[(z-R)/\Delta R]$. We also assume the range bin width is small enough such that the sample volume can be approximated by $V \approx A_{beam}\Delta R$, where A_{beam} is the cross-sectional area of the laser beam. These assumptions yield

$$\langle P(R)\rangle = \beta C(R)\int_{A_{beam}} I_{tx}(x,y,R)dA\int_R^{R+\Delta R} dz. \tag{11}$$

Defining the transmitted power over the aperture $P_{tx} = \int_{A_{beam}} I_{tx}(x,y,z)dA$, the classical volume backscatter lidar equation is recovered:

$$\langle P(R)\rangle = P_{tx}\beta\Delta R C(R). \tag{12}$$

https://doi.org/10.5194/egusphere-2026-3698
Preprint. Discussion started: 2 July 2026

4.1.1 Discussion of key assumptions

The derivation relies on a set of assumptions that determine the validity of the continuum volume interpretation. In this section, the key assumptions are restated explicitly and identify cloud regimes and instrument configurations in which they break down, resulting in deviations from the classical volume backscatter formulation.

1. **High-occupancy limit** – The law of large numbers underlies the transition from a discrete-particle to continuum representation of the volume backscatter lidar equation. In particular, it justifies replacing the sum over individual scatterer contributions with its expectation in the limit of large particle numbers within the measurement volume. This requires the scattering particles within the volume to be sufficiently large in count, independent, and identically distributed. However, this regime may not be satisfied in optically thin clouds or precipitation, where the particle number density is low and the received signal remains strongly influenced by fluctuations in the discrete particle configuration.

2. **Local homogeneity** – A second requirement is that the cloud field is locally homogeneous relative to the instrument resolution. This allows particle position and size statistics to be treated as separable within the measurement volume. However, this condition is not guaranteed in heterogeneous cloud regions, such as entrainment zones and cloud boundaries, where droplet size is affected by the mixing of entrained dry air (Lehmann et al., 2009).

Another important implicit condition is the linear superposition of single-particle scattering contributions, such that multiple-scattering effects are negligible. Multiple scattering violates this condition by making the received signal depend on coupled photon paths rather than independent single-particle contributions, inducing statistical dependence in particle-scattering events. It can also increase effective optical path lengths and spatially redistribute scattered energy, thereby smoothing the measured return from heterogeneous cloud features. This condition is especially important in optically thick media, such as dense liquid-water clouds, where the high particle occupancy required for the volumetric approximation may be satisfied even as the single-scattering assumption breaks down.

While the breakdown of linear superposition must be considered in these regimes, it does not undercut the results in this study. Rather, the significance of this discrete-to-continuum formulation is that it provides a foundation for understanding and characterizing lidar measurements in clouds, even when the scattering regime is not easily classified as single or multiple. Moreover, the ultra-high-resolution architecture provides a pathway for investigating multiple-scattering effects in clouds at scales that would otherwise be obscured by conventional averaging.

Together, these assumptions define a regime in which the lidar equation can be interpreted as a homogeneous, continuum approximation of an underlying discrete scattering process. In this regime, the effects of individual particle configurations on the measurement (i.e., finite scattering and heterogeneity) are suppressed. Outside of this regime, deviations arise, leading to departures from the ensemble-mean description. However, while the preceding discussion identifies the physical conditions under which the continuum approximation fails, it does not quantify the resulting error introduced when the volume backscatter formulation is applied outside its validity regime. This motivates a statistical formulation of the variability induced by finite-particle occupancy.

https://doi.org/10.5194/egusphere-2026-3698
Preprint. Discussion started: 2 July 2026

4.2 Finite-sampling variability and the continuum limit

In this section, we derive finite-sampling variability: an expression that quantifies how strongly a lidar measurement is influenced by the discreteness of the underlying particle field. In high-occupancy regimes, numerous particle-scattering contributions are averaged, such that the cumulative return is well represented by the ensemble mean and exhibits little realization-to-realization variability. In sparse regimes, the received signal remains strongly conditioned by the particular finite-particle configuration sampled by the instrument, leading to strong fluctuations between realizations. Therefore, the resulting signal variability provides a quantitative indicator of where the measurement lies along the transition from discrete-particle sampling to continuum-volume scattering. It is worth noting that this analysis focuses specifically on the effect of finite-particle occupancy on lidar measurements, while the influence of heterogeneous scatter structure is reserved for future work.

The process of sampling a volume of discrete particles can be treated as a series of independent samples of the random variables contributing to the lidar signal. We begin by defining the coefficient of variation of received power as the metric for finite-sampling variability:

$$\epsilon(R|N) \triangleq \frac{\sqrt{\mathrm{Var}[P(R|N)]}}{\mathbb{E}[P(R|N)]}. \tag{13}$$

where Var denotes variance and $\mathbb{E}$ the expectation value. Coefficient of variation is a suitable metric for finite-sampling variability because it describes the relative spread of possible received signals conditioned on different realizations of the particle field. In this sense, $\epsilon(R|N)$ is not only a variability estimator, but also a regime indicator. Small values indicate that many independent scattering contributions constrain the measurement near its ensemble mean, while larger values indicate that the measurement retains information about the discreteness of the sampled particle configuration.

Plugging in the discrete definition from Eq. 3, we rewrite the finite-sampling variability term as

$$\epsilon(R|N) = \frac{\sqrt{\mathrm{Var}\left[\sum_{i=1}^{N} I(x_i,y_i,z_i)\frac{d\sigma_b}{d\Omega}(s)\right]}}{\mathbb{E}\left[\sum_{i=1}^{N} I(x_i,y_i,z_i)\frac{d\sigma_b}{d\Omega}(s)\right]}. \tag{14}$$

Under the assumption that particle contributions are independent and identically distributed:

$$\epsilon(R|N) = \frac{1}{\sqrt{N}}\frac{\sqrt{\mathrm{Var}\left[I(x,y,z)\frac{d\sigma_b}{d\Omega}(s)\right]}}{\mathbb{E}\left[I(x,y,z)\frac{d\sigma_b}{d\Omega}(s)\right]}. \tag{15}$$

Assuming the irradiance field and particle backscatter contributions are statistically independent,

$$\epsilon(R|N) = \frac{1}{\sqrt{N}}\frac{\sqrt{\mathrm{Var}(I)\mathbb{E}\left[\frac{d\sigma_b}{d\Omega}\right]^2 + \mathrm{Var}\left(\frac{d\sigma_b}{d\Omega}\right)\mathbb{E}[I]^2 + \mathrm{Var}(I)\mathrm{Var}\left(\frac{d\sigma_b}{d\Omega}\right)}}{\mathbb{E}[I]\mathbb{E}\left[\frac{d\sigma_b}{d\Omega}\right]}, \tag{16}$$

we can express the finite-sampling variability in terms of coefficients of varation, which yields

$$\epsilon(R|N) = \frac{1}{\sqrt{N}}\sqrt{\mathrm{CV}_I^2 + \mathrm{CV}_\sigma^2 + \mathrm{CV}_I^2\mathrm{CV}_\sigma^2}, \tag{17}$$

https://doi.org/10.5194/egusphere-2026-3698
Preprint. Discussion started: 2 July 2026

where

$$\mathrm{CV}_I \triangleq \frac{\sqrt{\mathrm{Var}(I)}}{\mathbb{E}[I]} \tag{18}$$

and

$$\mathrm{CV}_\sigma \triangleq \frac{\sqrt{\mathrm{Var}\left(\frac{d\sigma_b}{d\Omega}\right)}}{\mathbb{E}\left[\frac{d\sigma_b}{d\Omega}\right]} \tag{19}$$

are the coefficients of variation associated with the irradiance field and particle backscatter contributions, respectively. Although finite-sampling variability is not intended as a comprehensive uncertainty metric, it can be interpreted as an estimate of the uncertainty associated with applying the volume approximation in finite-particle regimes. The uncertainty therefore decreases as $N^{-1/2}$, while its amplitude is scaled by the relative variances of the irradiance field and particle backscatter properties. Note that separating the irradiance field from the particle backscatter contribution assumes that the field is largely insensitive to the presence of particles. This assumption may not hold in all regimes when diffractive effects significantly perturb the irradiated field.

To illustrate the implications of finite-sampling variability, we performed a simple numerical experiment using representative cloud and instrument parameters. A synthetic cloud particle population was generated from a standard droplet size distribution, i.e., gamma distribution representing size-resolved concentration: $n'(D) = N_0'\beta^\alpha\Gamma(\alpha)^{-1}D^{\alpha-1}\exp(-\beta D)$, where N_0' is the number concentration, D is the particle diameter, β and α are the respective rate and shape parameters, and $\Gamma(\alpha)$ is the gamma function. The lidar transmitter was modeled as a Gaussian beam with realistic divergence and pulse width for the system described here and range resolution of $0.1\,\mathrm{m}$.

The simulation was used to estimate finite-sampling variability as a function of range, integration time, sample-volume size, and particle concentration. Eq. 17 shows that beam-irradiance and particle-backscatter variation (i.e., $\mathrm{CV_I}$ and CV_σ) influence finite-sampling variability. In addition, the number of particles within the measurement volume strongly affects variability, which is dictated by particle number density and integration volume (i.e., beam width, range-bin size, and integration time). Note that the number of contributing, statistically independent particles is not directly related to the number of integrated laser shots due to shot-to-shot correlative effects and is instead defined by the rate at which particles pass in and out of the sample volume. In this simulation, this replacement process was modeled using a particle-transport advection term, though this concept will require more investigation for a more comprehensive description.

The results in Fig. 3 reinforce the key predictions of Eq. 17: finite-sampling variability decreases with increasing integration time, increasing particle concentration, and increasing sample volume. The integration-time dependence follows the familiar $N^{-1/2}$ scaling, where longer averaging periods effectively increase the number of independent particle contributions to the measurement. However, the mapping between N and integration time is conditional. Variability is governed by the number of independent particle contributions, which, under realistic conditions, depends on the temporal evolution of the particle field within the sample volume. In this example, particle replacement is modeled using an idealized advection framework. Variability also decreases with range because beam spreading increases the measurement volume and therefore the expected particle count. At the ultra-high-range resolution obtained with this system, the expected particle population within the measurement volume

https://doi.org/10.5194/egusphere-2026-3698
Preprint. Discussion started: 2 July 2026

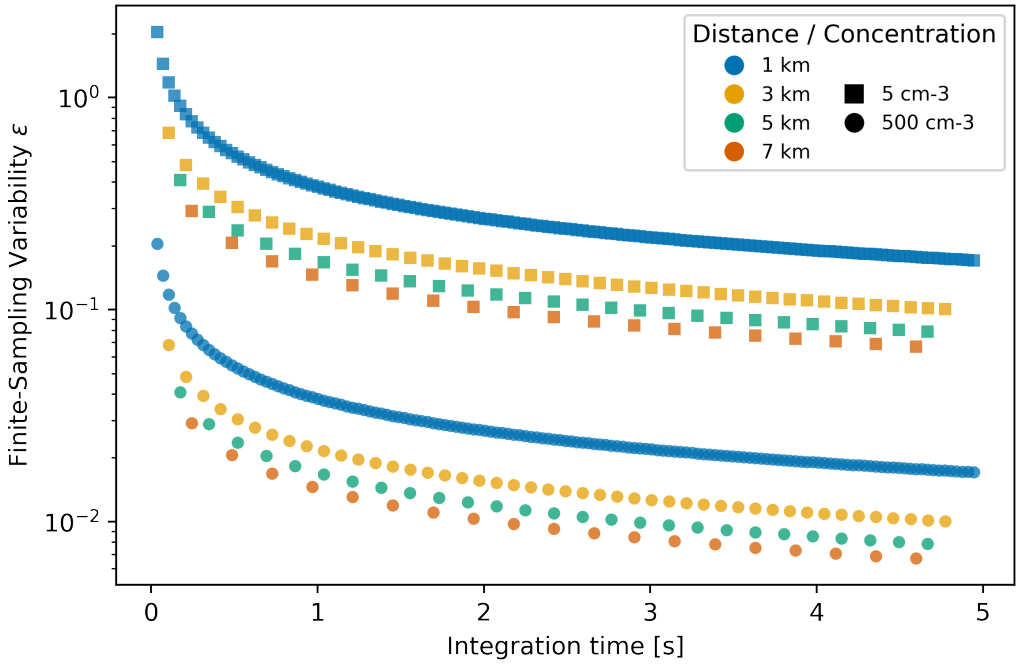

Figure 3. Simulated finite-sampling variability predicted by Eq. 17 for an idealized advecting-particle-replacement model. Results are shown as functions of integration time, range, and particle concentration, illustrating the transition from finite-particle sampling to a volume-scattering regime.

is sufficiently large for typical liquid-water-cloud concentrations ($\sim 500\,\mathrm{cm}^{-3}$), such that the cloud behaves like a continuous medium after less than a second of integration time, i.e., variability is smaller than 5%. In contrast, lower-concentration regimes such as drizzle ($\sim 5\,\mathrm{cm}^{-3}$) require substantially longer integration periods to approach a volume-scattering regime.

Another important constraint is that averaging can only reduce variability while the cloud remains statistically stationary. In moderate- to low-particle-density environments, the integration times required to reduce finite-sampling variability may become comparable to or exceed the timescales over which cloud properties evolve. This same concept extends to the spatial dimension as well: while increasing the sample volume reduces variability in finite-sampling regimes, it does so at the cost of smoothing any heterogeneous fine-scale structure that may be present. As particle concentrations decrease, the assumptions underlying the volume backscatter lidar equation become increasingly difficult to justify, motivating a discrete-particle interpretation of the measurement. While this may be interpreted as a barrier to lidar performance, it also presents a unique opportunity for new measurement techniques that move beyond the volumetric-lidar convention and enable retrievals that exploit finite-scattering effects in clouds. In the next section, we demonstrate two retrievals that achieve this by treating observations as single particles rather than volume-averaged quantities.

https://doi.org/10.5194/egusphere-2026-3698
Preprint. Discussion started: 2 July 2026

5 Particle-resolved retrievals

Having established that the measurement process in clouds can enter a discrete-scattering regime, we now demonstrate retrievals that operate directly on individual scattering events rather than a volume-averaged approximation. This enables two complementary demonstrations: first, streak-like signatures associated with precipitating hydrometeors are used to infer droplet kinematics, including vertical velocity; second, a flux-estimation framework operating at single-particle precision explicitly accounts for detector nonlinearities in high-photon-count regimes. Together, these examples illustrate how particle-resolved measurements can be used not only to identify individual hydrometeors, but also to begin constructing quantitative retrievals of their physical properties.

5.1 Single-droplet velocity retrievals

Processed observations of individual rain droplets during a precipitation event are presented. Fig. 4 shows a measurement consistent with virga, appearing as a wispy feature descending from approximately $3 - 1.5\,\mathrm{km}$ beneath a mid-level cloud, with precipitation persisting throughout the acquisition period. When examined at higher resolution, individual hydrometeors become resolvable as discrete, streak-like clusters that are largely oriented parallel to one another (Fig. 4b-c). These streaks are interpreted as precipitating droplets repeatedly sampled as they traverse the laser beam, producing elongated signatures whose geometry reflects the intersection between particle trajectories and the sample volume. Because of the laser's high repetition rate, a single droplet can be sampled multiple times during a single beam crossing. For instance, a droplet at $\sim 1.8\,\mathrm{km}$ range with a transverse velocity of $2\,\mathrm{m\,s^{-1}}$ may be sampled thousands of times, depending on its chord-length intersection with the beam. Here, "transverse" refers to motion perpendicular to the beam axis, and the beam axis is assumed to be vertical.

The streak geometry contains information about droplet kinematics that can be leveraged. First, the streak slope encodes the ratio between vertical displacement (defined along the beam axis) and residence time in the beam. To estimate these slopes, a Gaussian mixture model was applied to represent each cluster, as the observed streaks are approximately elliptical in shape. The major-axis orientation of each fitted component provides an estimate of the streak's slope, from which the vertical velocity of each droplet can be inferred. The resulting velocity estimates are shown in Fig. 4d.2, where fitted ellipses and derived vertical velocities are overlaid.

Second, the observed streak length encodes the droplet's residence time within the beam, which is governed by the beam geometry, the droplet's transverse velocity, and the intersection path length. This relationship may be further modulated by nonuniform beam illumination and variations in scattering behavior during transit. While isolating beam geometry effects is nontrivial, this relationship motivates engineering future lidar architectures and methods for retrieving transverse velocities.

This analysis demonstrates that discrete hydrometeor signatures can be used to directly recover particle-scale kinematics from lidar data. While the present implementation is applied to a limited scene, the same approach can be extended to larger datasets to construct statistically robust distributions of droplet vertical velocities.

https://doi.org/10.5194/egusphere-2026-3698
Preprint. Discussion started: 2 July 2026

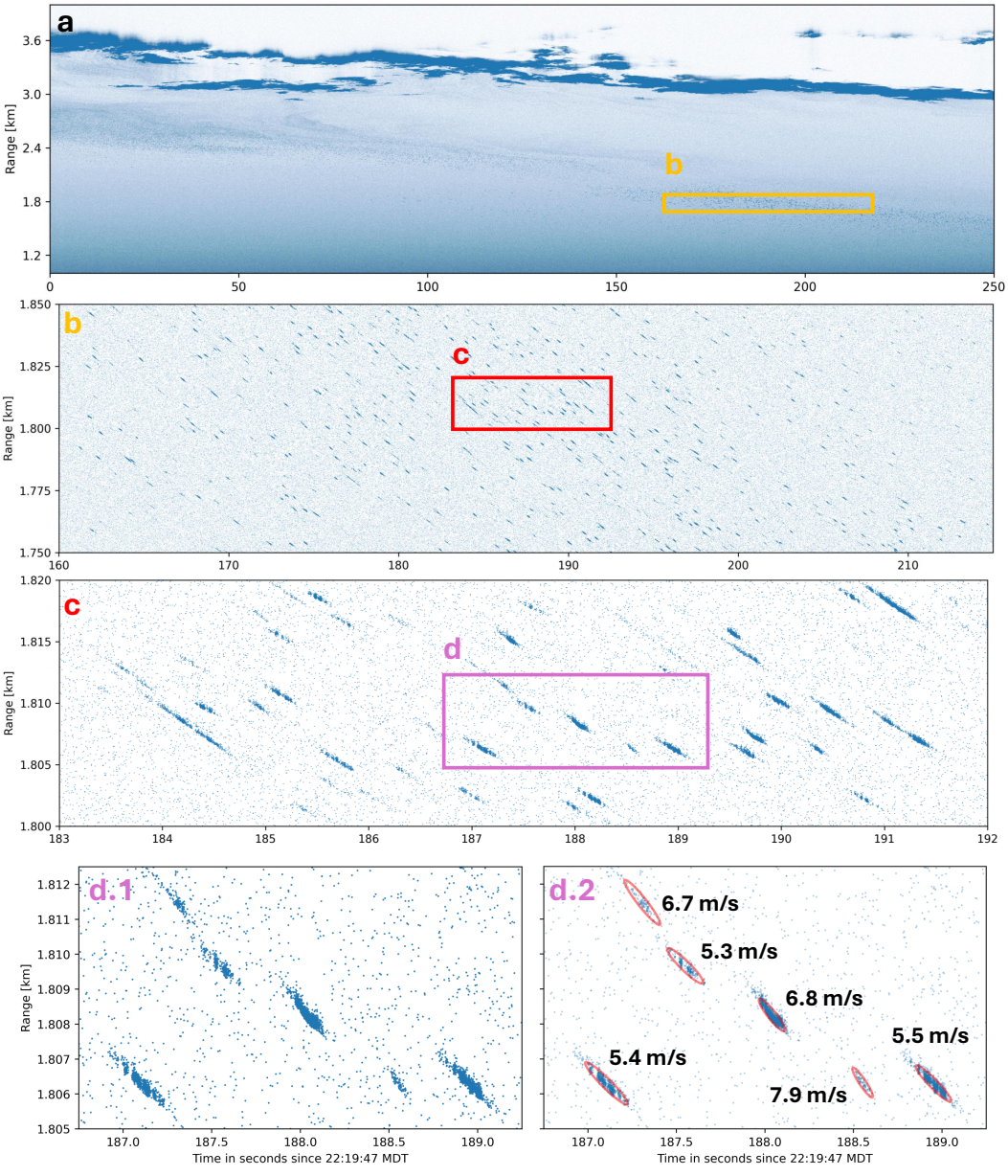

Figure 4. Ultra-high-resolution lidar observation of a descending precipitation feature beneath a mid-level cloud, consistent with virga. Panel (a) shows the broader time-range scene, while panels (b), (c), and (d.1) show enlarged regions where individual hydrometeors appear as discrete, streak-like clusters, consistent with repeated sampling as particles traverse the laser beam. Panel (d.2) shows fitted ellipses used to estimate streak orientation, with the inferred vertical velocities overlaid.

https://doi.org/10.5194/egusphere-2026-3698
Preprint. Discussion started: 2 July 2026

5.2 Single-particle flux retrievals

Observations of individual hydrometeors can enable flux-based retrieval methods that approach single-particle scales. Most lidar retrievals rely on inverting measured photon flux to infer physical properties, such as particle concentration or size, making accurate flux estimation critical in the single-particle regime. Here, we demonstrate a processing framework designed to estimate flux at time-tag precision under conditions where detector nonlinearities become significant.

The method was applied to a single hydrometeor near cloud base, as shown in Fig. 5. At higher magnification, the scene contains discrete photon clusters consistent with many individual hydrometeors (Fig. 5b). A single target is windowed and shown in Fig. 5c.1, where its high photon count and dense clustering make it representative of typical hydrometeor observations and suitable for evaluating flux estimation.

The data in Fig. 5c.1 were processed using maximum likelihood estimation (MLE), which enables efficient inference from sparse, clustered photon statistics while preserving time-tag resolution. The model was based on a Poisson photon-counting process modified to incorporate detector saturation effects, from Kirchhoff et al. (2025). This is particularly important for single-photon avalanche photodiode systems, where finite, nonparalyzable deadtime leads to nonlinear response at high photon count rates ($> 10\,\mathrm{MHz}$). In this regime, many observed hydrometeors exceed the detector's linear dynamic range, making explicit correction for deadtime-induced bias necessary. Rather than avoid saturation by reducing optical power, which would degrade signal-to-noise ratio, the detector deadtime response was incorporated directly into the likelihood model.

To initialize the MLE fitting routine, the data in Fig. 5c.1 were reduced to one-dimensional range-resolved fluxes, shown in Fig. 5c.2. This one-dimensional fitting approach was chosen for simplicity while preserving the essential features needed for the demonstration. The plot shows instantaneous flux values that exceed 100 MHz, well above the detector saturation threshold. In contrast, binning over a $10\,\mathrm{m} \times 10\,\mathrm{s}$ window yields a single averaged estimate of $\sim$7 MHz (labeled as "Coarse" in the figure panel). In regions of even lower particle density, such as precipitation, averaging over the particle would induce flux estimates that are orders of magnitude lower, rendering the particle undetectable and the user entirely unaware of the flux regime the detector was exposed to. We then used the MLE framework to parametrically fit the training data, with the result shown in Fig. 5c.2. The fit explicitly accounts for saturation-induced loss of counts in the estimate. This result is consistent with the prior demonstration of deadtime-aware photon inference at sub-meter spatial and sub-second temporal resolution in Kirchhoff et al. (2025).

Taken together, these results demonstrate that flux estimates at conventional lidar resolutions should not be expected to produce accurate estimates of true photon flux in clouds and precipitation. This is because averaging over sparse, high-flux particles will result in apparent measurements of low flux that inaccurately represent the true flux and nonlinear effects experienced by the detector. This outcome represents a step towards accurate flux-resolved lidar retrievals at scales more consistent with cloud microphysics.

https://doi.org/10.5194/egusphere-2026-3698
Preprint. Discussion started: 2 July 2026

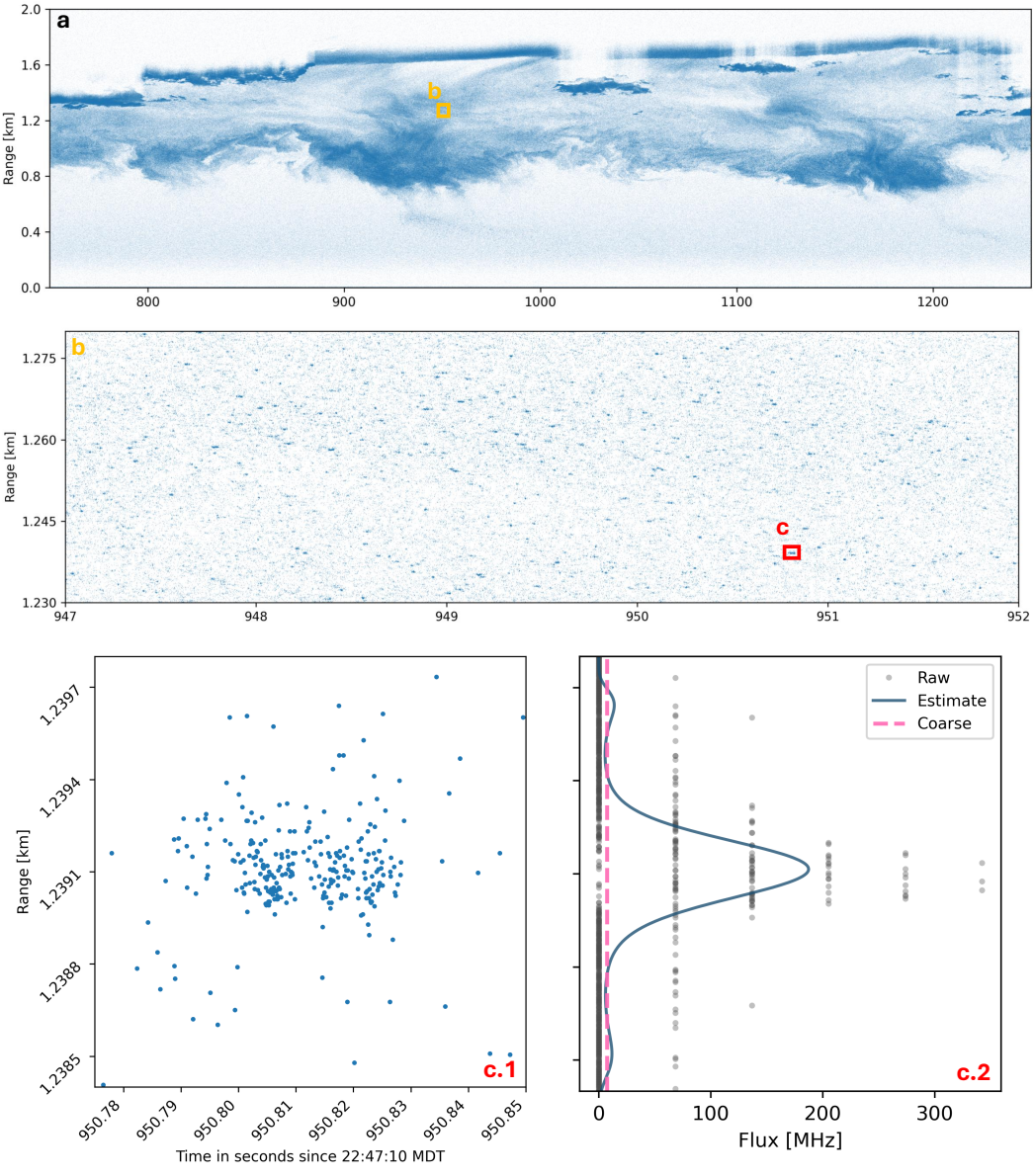

Figure 5. Single-hydrometeor flux estimation from ultra-high-resolution photon-counting data. Panels (a) and (b) show the broader cloud-base scene and an enlarged region containing discrete photon clusters consistent with individual hydrometeors. Panel (c.1) shows the selected hydrometeor used for flux estimation at native resolution (4 mm × 70 µs). Panel (c.2) compares the MLE range-resolved photon-flux estimate, along with the coarse (10 m × 10 s) binned value.

https://doi.org/10.5194/egusphere-2026-3698
Preprint. Discussion started: 2 July 2026

6 Conclusions

In this study, we interrogated the conditions under which cloud-lidar measurements can be interpreted through the conventional volumetric framework. First, we used ultra-high-resolution lidar observations of clouds to reveal fine-scale discrete scattering features, i.e., heterogeneous structures and finite-particle scattering. This motivated a stochastic description of cloud-lidar measurements, framing returns as the cumulative backscatter from individual hydrometeors. By deriving the classical volume backscatter lidar equation from this formulation, we highlighted how homogeneous and continuum sampling are particular conditions necessary for the volumetric approximation to be valid. We also discussed specific cloud conditions and instrument properties that can fall outside of these conditions, and investigated the received-signal variability expected in finite-sampling regimes. Lastly, we showcased examples of lidar retrievals that move beyond the volumetric interpretation and exploit the discreteness uncovered by ultra-high-resolution lidar, thus enabling hydrometeor-resolved estimates of kinematics and flux in sparse clouds and precipitation.

This work motivates a need for a more unified framework for lidar measurements in sparse or transitional cloud regimes, where neither purely continuous-media assumptions nor coarse averaging are strictly valid. In such cases, observables must be interpreted through models that explicitly account for individual particle-scattering contributions and their statistical nature. The results of this work suggest that lidar measurements of clouds and precipitation may not be as straightforward as previously thought, but they also open the door to new possibilities for lidar design and retrievals that were previously out of reach. Because the observed scattering regime depends on both the cloud microphysical properties and instrument configuration, future lidar designs may be able to leverage this relationship to isolate discrete-scattering effects and extract new information about the environment.

Conventional lidar resolutions will continue to be used in cloud sensing. The ultra-high-resolution approach presented here complements those measurements by providing a mechanism to better understand the uncertainties and validity of volumetric lidar regimes while motivating new approaches. Although the present work focuses on illustrative cloud examples, the same principles extend to other sparse or heterogeneous particulate media, like smoke plumes and aerosol layers.

Code and data availability. The code and data used for producing the figures in this manuscript are publicly available on Zenodo at https://doi.org/10.5281/zenodo.20753336 (Kirchhoff et al., 2026). Processing code and methods are available upon request.

Author contributions. GJK, MH, and JPT conceived and designed the study. GJK and MH designed the lidar. GJK assembled the lidar with contributions from BHG. GJK and BHG tested the lidar. GJK collected the data. GJK and MH developed the theoretical framework, data-analysis and signal-processing methods. GJK processed the data and wrote the original paper draft. MH and JPT supervised the work. All authors reviewed and edited the manuscript.

https://doi.org/10.5194/egusphere-2026-3698
Preprint. Discussion started: 2 July 2026

Competing interests. The authors declare no competing interests.

Acknowledgements. This work was supported by a NASA Space Technology Research Grant Program (NSTGRO). The lead author would like to acknowledge Amin Nehrir and Xiaoli Sun for their guidance and support through the NSTGRO research fellowship and development of this research. The authors would also like to thank Robert Stillwell, Scott Spuler, Rory Barton-Grimley, Kevin Sacca, and Alexandra Wise for their support and input during the lidar system design and build; Samuel Miller for helping with instrument operations; and Nate Coyle for machine shop assistance at CU Boulder. ChatGPT was used to assist with proofreading, language editing, and organization. All content was reviewed, verified, and edited by the authors, who take full responsibility for the manuscript and its figures.

https://doi.org/10.5194/egusphere-2026-3698
Preprint. Discussion started: 2 July 2026

References

Alkasem, A., Szczap, F., Cornet, C., Shcherbakov, V., Gour, Y., Jourdan, O., Labonnote, L. C., and Mioche, G.: Effects of cirrus heterogeneity on lidar CALIOP/CALIPSO data, J. Quant. Spectrosc. Radiat. Transf., 202, 38–49, https://doi.org/10.1016/j.jqsrt.2017.07.005, 2017.

Arola, A., Lipponen, A., Kolmonen, P., Virtanen, T. H., Bellouin, N., Grosvenor, D. P., Gryspeerdt, E., Quaas, J., and Kokkola, H.: Aerosol effects on clouds are concealed by natural cloud heterogeneity and satellite retrieval errors, Nat. Commun., 13, 7357, https://doi.org/10.1038/s41467-022-34948-5, 2022.

Barton-Grimley, R. A., Stillwell, R. A., and Thayer, J. P.: High resolution photon time-tagging lidar for atmospheric point cloud generation, Opt. Express, 26, 26 030–26 044, https://doi.org/10.1364/OE.26.026030, 2018.

Beals, M. A., Fugal, J. P., Shaw, R. A., Lu, J., Spuler, S. M., and Stith, J. L.: Holographic measurements of inhomogeneous cloud mixing at the centimeter scale, Science, 350, 87–90, https://doi.org/10.1126/science.aab0751, 2015.

Becker, W.: Advanced Time-Correlated Single Photon Counting Techniques, vol. 81 of *Springer Series in Chemical Physics*, Springer, Berlin and Heidelberg, ISBN 978-3-540-26047-9, https://doi.org/10.1007/3-540-28882-1, 2005.

Beswick, K., Baumgardner, D., Gallagher, M., Raga, G. B., Minnis, P., Spangenberg, D. A., Volz-Thomas, A., Nedelec, P., and Wang, K.-Y.: Properties of small cirrus ice crystals from commercial aircraft measurements and implications for flight operations, Tellus B Chem. Phys. Meteorol., 67, 27 876, https://doi.org/10.3402/tellusb.v67.27876, 2015.

Bissonnette, L. R.: Lidar and Multiple Scattering, in: Lidar: Range-Resolved Optical Remote Sensing of the Atmosphere, edited by Weitkamp, C., vol. 102 of *Springer Series in Optical Sciences*, pp. 43–103, Springer, New York, NY, https://doi.org/10.1007/0-387-25101-4_3, 2005.

Bohren, C. F. and Huffman, D. R.: Absorption and Scattering of Light by Small Particles, Wiley, New York, NY, ISBN 9780471293408, https://doi.org/10.1002/9783527618156, 1983.

CALIPSO Science Team and Lidar Science Working Group: CALIPSO Quality Statements: Lidar Level 1B Profile Products, Version Releases 2.01 and 2.02, Tech. rep., NASA Langley Research Center Atmospheric Science Data Center, https://asdc.larc.nasa.gov/documents/calipso/quality_summaries/CALIOP_L1ProfileProducts_2.01.pdf, last access: 14 June 2026, 2007.

Comstock, J. M. and Sassen, K.: Retrieval of cirrus cloud radiative and backscattering properties using combined lidar and infrared radiometer (LIRAD) measurements, J. Atmos. Ocean. Technol., 18, 1658–1673, https://doi.org/10.1175/1520-0426(2001)018<1658:ROCCRA>2.0.CO;2, 2001.

Crosbie, E., Hair, J. W., Nehrir, A. R., Ferrare, R. A., Hostetler, C., Shingler, T., Harper, D., Fenn, M., Collins, J., Barton-Grimley, R., Collister, B., Thornhill, K. L., Voigt, C., Kirschler, S., and Sorooshian, A.: A method to retrieve mixed-phase cloud vertical structure from airborne lidar, Atmos. Meas. Tech., 18, 2639–2658, https://doi.org/10.5194/amt-18-2639-2025, 2025.

Eloranta, E. W.: Practical model for the calculation of multiply scattered lidar returns, Appl. Opt., 37, 2464–2472, https://doi.org/10.1364/AO.37.002464, 1998.

Fan, J., Wang, Y., Rosenfeld, D., and Liu, X.: Review of aerosol–cloud interactions: mechanisms, significance, and challenges, J. Atmos. Sci., 73, 4221–4252, https://doi.org/10.1175/JAS-D-16-0037.1, 2016.

Fernald, F. G.: Analysis of atmospheric lidar observations: Some comments, Appl. Opt., 23, 652–653, https://doi.org/10.1364/AO.23.000652, 1984.

https://doi.org/10.5194/egusphere-2026-3698
Preprint. Discussion started: 2 July 2026

Flynn, D., Sivaraman, C., Comstock, J., and Zhang, D.: Micropulse Lidar Cloud Mask (MPLCMASK) Value-Added Product for the Fast-Switching Polarized Micropulse Lidar Technical Report, Tech. Rep. DOE/SC-ARM/TR-098, DOE Office of Science Atmospheric Radiation Measurement (ARM) User Facility, United States, https://doi.org/10.2172/1019283, 2020.

Glienke, S., Kostinski, A. B., Shaw, R. A., Larsen, M. L., Fugal, J. P., Schlenczek, O., and Borrmann, S.: Holographic observations of centimeter-scale nonuniformities within marine stratocumulus clouds, J. Atmos. Sci., 77, 499–512, https://doi.org/10.1175/JAS-D-19-0164.1, 2020.

Griesche, H. J., Seifert, P., Engelmann, R., Radenz, M., Hofer, J., Althausen, D., Walbröl, A., Barrientos-Velasco, C., Baars, H., Dahlke, S., Tukiainen, S., et al.: Cloud micro- and macrophysical properties from ground-based remote sensing during the MOSAiC drift experiment, Sci. Data, 11, 505, https://doi.org/10.1038/s41597-024-03325-w, 2024.

Hu, Y., Winker, D., Vaughan, M., Lin, B., Omar, A., Trepte, C., Flittner, D., Yang, P., Nasiri, S. L., Baum, B., Holz, R., Sun, W., Liu, Z., Wang, Z., Young, S., Stamnes, K., Huang, J., and Kuehn, R.: CALIPSO/CALIOP cloud phase discrimination algorithm, J. Atmos. Ocean. Technol., 26, 2293–2309, https://doi.org/10.1175/2009JTECHA1280.1, 2009.

IPCC: Climate Change 2021: The Physical Science Basis. Contribution of Working Group I to the Sixth Assessment Report of the Intergovernmental Panel on Climate Change, Cambridge University Press, Cambridge, United Kingdom and New York, NY, USA, https://doi.org/10.1017/9781009157896, 2021.

Jimenez, C., Ansmann, A., Engelmann, R., Donovan, D., Malinka, A., Schmidt, J., Seifert, P., and Wandinger, U.: The dual-field-of-view polarization lidar technique: a new concept in monitoring aerosol effects in liquid-water clouds – theoretical framework, Atmos. Chem. Phys., 20, 15 247–15 263, https://doi.org/10.5194/acp-20-15247-2020, 2020.

Kirchhoff, G. J., Hayman, M., Marais, W. J., Thayer, J. P., and Barton-Grimley, R. A.: Development of a photon-counting deadtime noise model that extends dynamic range and resolution in atmospheric lidar, Appl. Opt., 64, 4568–4581, https://doi.org/10.1364/AO.543305, 2025.

Kirchhoff, G. J., Hayman, M., Thayer, J. P., and Garby, B. H.: Plotting scripts and processed data for "Resolving heterogeneous structure and finite scattering in clouds and precipitation with ultra-high-resolution lidar", https://doi.org/10.5281/zenodo.20753336, 2026.

Knyazikhin, Y., Marshak, A., Larsen, M. L., and Wiscombe, W. J.: Small-Scale Drop Size Variability: Impact on Estimation of Cloud Optical Properties, J. Atmos. Sci., 62, 2555–2567, https://doi.org/10.1175/JAS3488.1, 2005.

Kostinski, A. B. and Shaw, R. A.: Scale-Dependent Droplet Clustering in Turbulent Clouds, J. Fluid Mech., 434, 389–398, https://doi.org/10.1017/S0022112001004025, 2001.

Last, G. and Penrose, M.: Lectures on the Poisson Process, vol. 7 of *Institute of Mathematical Statistics Textbooks*, Cambridge University Press, Cambridge, https://doi.org/10.1017/9781316104477, 2017.

Lehmann, K., Siebert, H., and Shaw, R. A.: Homogeneous and Inhomogeneous Mixing in Cumulus Clouds: Dependence on Local Turbulence Structure, J. Atmos. Sci., 66, 3641–3659, https://doi.org/10.1175/2009JAS3012.1, 2009.

Measures, R. M.: Laser Remote Sensing: Fundamentals and Applications, Wiley-Interscience, New York, ISBN 978-0-471-08193-7, 1984.

Miles, N. L., Verlinde, J., and Clothiaux, E. E.: Cloud droplet size distributions in low-level stratiform clouds, J. Atmos. Sci., 57, 295–311, https://doi.org/10.1175/1520-0469(2000)057<0295:CDSDIL>2.0.CO;2, 2000.

Morrison, H., van Lier-Walqui, M., Fridlind, A. M., Grabowski, W. W., Harrington, J. Y., Hoose, C., Korolev, A., Kumjian, M. R., Milbrandt, J. A., Pawlowska, H., Posselt, D. J., Prat, O. P., Reimel, K. J., Shima, S.-I., van Diedenhoven, B., and Xue, L.: Confronting the Challenge of Modeling Cloud and Precipitation Microphysics, J. Adv. Model. Earth Syst., 12, e2019MS001 689, https://doi.org/10.1029/2019MS001689, 2020.

https://doi.org/10.5194/egusphere-2026-3698
Preprint. Discussion started: 2 July 2026

National Research Council: Observing Weather and Climate from the Ground Up: A Nationwide Network of Networks, The National Academies Press, Washington, DC, ISBN 978-0-309-12986-2, https://doi.org/10.17226/12540, 2009.

Sassen, K.: The polarization lidar technique for cloud research: a review and current assessment, Bull. Am. Meteorol. Soc., 72, 1848–1866, https://doi.org/10.1175/1520-0477(1991)072<1848:TPLTFC>2.0.CO;2, 1991.

Shaw, R. A.: Particle-turbulence interactions in atmospheric clouds, Annu. Rev. Fluid Mech., 35, 183–227, https://doi.org/10.1146/annurev.fluid.35.101101.161125, 2003.

Thiede, B., Larsen, M. L., Nordsiek, F., Schlenczek, O., Bodenschatz, E., and Bagheri, G.: Highly Localised Droplet Clustering in Shallow Cumulus Clouds, https://doi.org/10.48550/arXiv.2502.19272, 2025.

Wang, Z. and Menenti, M.: Challenges and Opportunities in Lidar Remote Sensing, Front. Remote Sens., 2, 641 723, https://doi.org/10.3389/frsen.2021.641723, 2021.

Winker, D. M., Vaughan, M. A., Omar, A., Hu, Y., Powell, K. A., Liu, Z., Hunt, W. H., and Young, S. A.: Overview of the CALIPSO Mission and CALIOP Data Processing Algorithms, J. Atmos. Ocean. Technol., 26, 2310–2323, https://doi.org/10.1175/2009JTECHA1281.1, 2009.

Yang, F., Sua, Y. M., Louridas, A., Lamer, K., Zhu, Z., Luke, E., Huang, Y.-P., Kollias, P., Vogelmann, A. M., and McComiskey, A.: A time-gated, time-correlated single-photon-counting lidar to observe atmospheric clouds at submeter resolution, Remote Sens., 15, 1500, https://doi.org/10.3390/rs15061500, 2023.

Yang, F., Kostinski, A. B., Zhu, Z., Lamer, K., Luke, E., Kollias, P., Sua, Y. M., Hou, P., Shaw, R. A., and Vogelmann, A. M.: A single-photon lidar observes atmospheric clouds at decimeter scales: resolving droplet activation within cloud base, npj Clim. Atmos. Sci., 7, 92, https://doi.org/10.1038/s41612-024-00644-y, 2024.

Yang, F., Sua, Y. M., Zheng, Z., Anderson, J., Sadi, H. F., Yeom, J. M., Singh, S. P., Hou, P., Cantrell, W. H., Lewis, E. R., Kostinski, A. B., and Shaw, R. A.: High-resolution lidar observations of sedimentation-induced size sorting of droplets near a laboratory cloud top, Proc. Natl. Acad. Sci. U.S.A., 122, e2505421 122, https://doi.org/10.1073/pnas.2505421122, 2025.

Yeom, J. M., Helman, I., Prabhakaran, P., Anderson, J. C., Yang, F., Shaw, R. A., and Cantrell, W.: Cloud microphysical response to entrainment and mixing is locally inhomogeneous and globally homogeneous: evidence from the lab, Proc. Natl. Acad. Sci. U.S.A., 120, e2307354 120, https://doi.org/10.1073/pnas.2307354120, 2023.

Young, S. A., Vaughan, M. A., Garnier, A., Tackett, J. L., Lambeth, J. D., and Powell, K. A.: Extinction and optical depth retrievals for CALIPSO's Version 4 data release, Atmos. Meas. Tech., 11, 5701–5727, https://doi.org/10.5194/amt-11-5701-2018, 2018.

Zelinka, M. D., Myers, T. A., McCoy, D. T., Po-Chedley, S., Caldwell, P. M., Ceppi, P., Klein, S. A., and Taylor, K. E.: Causes of higher climate sensitivity in CMIP6 models, Geophys. Res. Lett., 47, e2019GL085 782, https://doi.org/10.1029/2019GL085782, 2020.

Zhu, Z., Yang, F., Kollias, P., Lamer, K., Luke, E., Mead, J. B., Sua, Y. M., Vogelmann, A. M., and McComiskey, A.: Peering into cloud physics using ultra-fine-resolution radar and lidar systems, Bull. Am. Meteorol. Soc., 105, E2010–E2025, https://doi.org/10.1175/BAMS-D-23-0032.1, 2024.